



# Spatial characterization of the flapping instability of a laminar liquid jet fragmented by a swirled gas co-flow

Maxime Kaczmarek, Rodrigo Osuna-Orozco, Peter Dearborn Huck, Alberto Aliseda, Peter Dearborn Huck, Nathanaël Machicoane

## ► To cite this version:

Maxime Kaczmarek, Rodrigo Osuna-Orozco, Peter Dearborn Huck, Alberto Aliseda, Peter Dearborn Huck, et al.. Spatial characterization of the flapping instability of a laminar liquid jet fragmented by a swirled gas co-flow. *International Journal of Multiphase Flow*, 2022, 152, pp.104056. 10.1016/j.ijmultiphaseflow.2022.104056 . hal-03634701

**HAL Id: hal-03634701**

**<https://hal.science/hal-03634701>**

Submitted on 11 Apr 2022

**HAL** is a multi-disciplinary open access archive for the deposit and dissemination of scientific research documents, whether they are published or not. The documents may come from teaching and research institutions in France or abroad, or from public or private research centers.

L'archive ouverte pluridisciplinaire **HAL**, est destinée au dépôt et à la diffusion de documents scientifiques de niveau recherche, publiés ou non, émanant des établissements d'enseignement et de recherche français ou étrangers, des laboratoires publics ou privés.

# Spatial characterization of the flapping instability of a laminar liquid jet fragmented by a swirled gas co-flow

Maxime Kaczmarek<sup>a</sup>, Rodrigo Osuna-Orozco<sup>b</sup>, Peter Dearborn Huck<sup>b</sup>,  
Alberto Aliseda<sup>b</sup>, Nathanaël Machicoane<sup>a</sup>

<sup>a</sup>*Univ. Grenoble Alpes, CNRS, Grenoble INP, LEGI, 38000 Grenoble, France*

<sup>b</sup>*University of Washington, Department of Mechanical Engineering, Seattle, WA 98105, USA*

---

## Abstract

A liquid jet destabilized by a co-flowing gas jet is subjected to several instabilities that are responsible for its fragmentation into a spray of fine droplets. At the large scale, the difference in the velocities of the gas and liquid phases lead to a meandering motion of the liquid jet called the flapping instability. Flapping is suspected to play a role in the spatio-temporal characteristics of the clouds of droplets further downstream, as it periodically brings a portion of the liquid phase away from the centerline and into the gas jet. While the scaling law determining the frequency associated to flapping has recently been proposed, a study of its spatial characteristics is lacking in the literature. Two-view high-speed back-lit imaging is used to obtain 3D time-resolved measurements of the liquid phase. The trajectories of the bulk of the liquid is computed using barycenter of the liquid presence. Such trajectories are phase averaged over many flapping periods to yield flapping orbits. In the regime of shear break-up atomization, a transition in the shape of the

---

*Email address:* `nathanael.machicoane@univ-grenoble-alpes.fr` (Nathanaël Machicoane)

flapping orbits, from planar to circular, is observed along variations of the gas-to-liquid dynamic pressure ratio (also called momentum ratio) as well as the swirl ratio (ratio of the azimuthal to longitudinal components of the gas jet). This is characterized using the shape factor of the flapping orbits, as well as the flapping amplitude. The latter is found to decrease with dynamic pressure ratio but is larger when swirl is added to the gas jet. The transition appears to be related to the formation of bags along the liquid jet, that originate from interfacial instabilities and opposes the existence of a preferential flapping direction.

*Keywords:* atomization, coaxial two-fluid atomizer, flapping, spray, gas swirl

---

## 1. Introduction

Atomization has a wide range of applications such as fuel mixing in combustion, cooling and coating processes, pharmaceutical sprays, powder production, or fire extinction. In such applications, the efficiency can be closely connected to the ability to control the spray characteristics, such as the droplet size distribution, the spray spatial spreading, or the frequency of droplet production [1; 2]. The fragmentation of a liquid jet by a coaxial gas jet is often described by the combination of two instabilities that disrupt the gas-liquid interface [3]. The Kelvin-Helmholtz instability is primarily responsible for the formation of the interfacial perturbations, stretched by the gas flow into ligaments or thin films. These liquid structures are accelerated and disintegrated into drops following the Rayleigh-Taylor instability. In addition, a large-scale instability lead to a meandering of the liquid jet into the

high-speed gas jet. This motion and the associated instability, first reported by [4], is referred to as flapping. Note that this meandering motion is also sometimes described as a sinusoidal or helicoidal instability [1; 5; 6; 7; 8; 9]. However, flapping remains to be measured in three dimensions (3D) to answer the open question of whether it is associated with planar or circular motions, which is the aim of this manuscript.

Flapping takes an important role in atomization since it is responsible for the sudden release of dense droplet clouds, periodically and with a certain level of spatial heterogeneity that needs to be better characterized and taken into account for modeling purposes. Recent work by Delon et al. [10], studied the flapping frequency experimentally and analytically to elucidate its physical origin as well as scaling laws with relevant parameters. Notably, they demonstrated the existence of a regime where the flapping instability is synchronized with a shear instability. In this regime, the flapping frequency is found to be linearly proportional to both the gas and liquid velocities. The present contribution focuses on the spatial characterization of the flapping instability, in a small sub-range of the parameter space within this regime. Moreover, the addition of angular momentum in the gas co-flow, or swirl, is also considered, as it is relevant in many applications of gas-assisted atomization. Early on, Hopfinger and Lasheras [11] demonstrated the existence of a critical value in the ratio of the gas jet angular to longitudinal velocity components, i. e. the swirl ratio, beyond which swirl addition drastically modifies the observed spray formation in the near-field. In parallel, researchers showed that the droplet population in the far-field of the spray was also affected when swirl was added to the gas jet beyond a critical value

[1; 12; 13]. It is only recently that a quantitative statistical study of the relevant near-field spray metrics was proposed along variations of the swirl ratio [14]. The changes in near-field and far-field metrics and the existence of critical values in the swirl ratio for which swirl addition is beneficial for atomization can be understood in the light of a vortex breakdown mechanism of the the gas jet. This mechanisms is similar to the one in single phase swirling jets [15]. In the case of a two-fluid atomizer, it happens downstream of the liquid jet. The consequence of vortex breakdown, in the form of a gas recirculation, was observed using high-speed synchrotron X-ray imaging [16]. Recently, [17] used Proper orthogonal decomposition (POD) to extract the flapping frequency and found that it can be increased in the presence of swirl. However, the effect of swirl on the flapping instability lacks a spatial characterization.

This manuscript reports on an experimental study of the near-field of coaxial two-fluid atomization using time-resolved 3D measurements based on two-view high-speed back-lit imaging. A new method to quantify the bulk liquid presence in the near-field is introduced. The method is tested in a wide range of gas-to-liquid dynamic pressure (also called momentum ratio in the literature) and swirl ratios, and offers an alternative to the initial spreading angles of the spray that is comparable to previous work [14]. In parallel, the previously available statistical description is complemented, in particular with a parametric description of the liquid core length distributions pertaining to its first three statistical moments. This method is then used to study flapping in a small range of parameters where measurements are feasible, i. e. for lower dynamic pressure ratios where longer liquid cores display a strong

temporal and spatial flapping signature. This contribution characterizes the spatial characteristics of the flapping instability at the onset of atomization of a laminar liquid jet by a turbulent gas jet that presents variable levels of swirl. Flapping orbits are retrieved using phase-averaging along many flapping periods and show a transition between planar and circular flapping motions, described quantitatively along the gas-to-liquid dynamic pressure and swirl ratios. Section 2 presents the experimental set-up and measurement methods. Sections 3 and 4 pertain to the statistical description of the liquid core length and the method to study how the liquid is redistributed in the near-field of a spray. Section 5 characterizes flapping in 3D, followed by a discussion and concluding remarks in Sec. 6 and 7.

## 2. Experimental setup

### 2.1. Coaxial two-fluid atomizer

The spray studied here is produced by an open-source canonical two-fluid coaxial atomizer (described in detail in [16; 18]). The atomizer is composed of an inner nozzle, referred to as liquid nozzle (inner diameter  $d_l = 2 \text{ mm}$  and outer diameter  $D_l = 3 \text{ mm}$ ), used to inject a laminar flow at a rate  $Q_l$ , and of a coaxial outer nozzle, referred to as gas nozzle (diameter  $d_g = 10 \text{ mm}$ ), used to inject the gas co-flow responsible for the atomization of the liquid jet (see Fig. 1a). Using the mean exit liquid velocity  $U_l = \frac{Q_l}{A_l}$  where  $A_l = \frac{\pi d_l^2}{4}$ , and the kinematic viscosity of water at 25°C  $\nu_l$ , the liquid Reynolds number is  $Re_l = \frac{d_l U_l}{\nu_l} \sim 1200$ .

The gas flow is guided into the gas nozzle by 8 inlets divided into two groups. The first group is composed of 4 inlets that are perpendicular to the

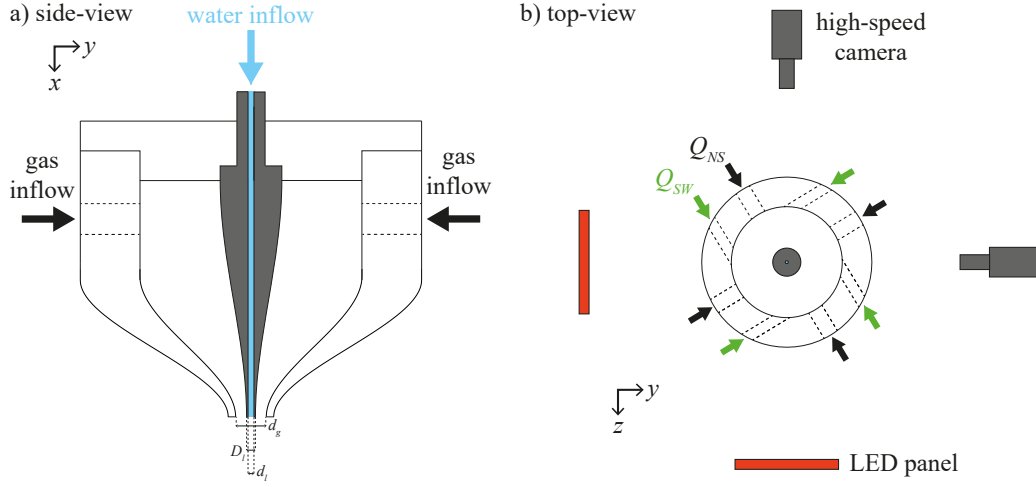


Figure 1: (color online) a) Longitudinal cut of the atomizer. Water is introduced in the center of the nozzle while gas is injected in an orthogonal horizontal plan. The indicated lengths are  $d_l = 2 \text{ mm}$ ,  $D_l = 3 \text{ mm}$ , and  $d_g = 10 \text{ mm}$ . b) Transverse cut of the atomizer. The gas is introduced in the nozzle through 8 inlets. Four of them are aligned on the atomizer's axis and produce a gas stream without angular momentum at a rate  $Q_{NS}$ , while the other four are shifted off the axis and produce a gas stream with angular momentum at a rate  $Q_{SW}$ . The liquid presence in the near-field is obtained in two transverse planes, perpendicular with respect to each other, thanks to two-view high-speed back-lit imaging.

axis of the atomizer (i. e. the longitudinal axis  $x$ , aligned with gravity), which produces a gas stream without angular momentum at a rate  $Q_{NS}$ , referred to as non-swirl gas flow rate. The second group is composed of 4 inlets that are shifted off the axis of the atomizer, and therefore create a gas stream with angular momentum at a rate  $Q_{SW}$ , referred to as swirl gas flow rate (see Fig. 1b). In order to study the impact of swirl addition on the behavior of the spray, the total gas flow rate, defined as  $Q_{Tot} = Q_{NS} + Q_{SW}$ , is kept constant for any given  $M$ , while the swirl ratio, defined as  $SR = Q_{SW}/Q_{NS}$  is varied between 0 to 0.75.

Using the mean exit gas velocity  $U_g = \frac{Q_{Tot}}{A_g}$  where  $A_g = \frac{\pi d_{eff}^2}{4}$  with  $d_{eff} = \sqrt{d_g^2 - D_l^2}$ , and the kinematic viscosity of air  $\nu_g$ , the gas Reynolds number  $Re_g = \frac{d_{eff} U_g}{\nu_g}$  ranges from  $1.4 \times 10^4$  to  $8.4 \times 10^4$ , depending on the total gas flow rate  $Q_{Tot}$ . Alternatively, variations of total gas flow rate are characterized by the gas-to-liquid dynamic pressure ratio  $M = \frac{\rho_g U_g^2}{\rho_l U_l^2}$  varying from 2 to 82, where  $\rho_i$  is the fluids' density and the subscripts  $l$  and  $g$  stand for the liquid and gas respectively ( $M$  is also referred to as gas-to-liquid momentum ratio in the literature).

A subset of the parameter space is studied in detail for the transition in shape of the flapping orbits (Sec. 5). The total gas flow rates, as well as the swirl ratio values are reported in Table 1. For every conditions, the atomization regimes correspond to shear break-up modes, following the nomenclature of [1], where the break-up events mostly follow large-scale motions of the liquid jet associated with the flapping instability (see Fig. 3a-b and movies in the Supplementary Materials). The shear break-up is associated with the prior creation of liquid membranes called bags on the liquid jet portion that



$Re_g$	$M$	$m$	$We_{d_l}$
13 600	2.11	0.88	15.4
16 400	3.10	0.72	22.7
21 400	5.27	0.56	39.1
31 400	11.3	0.38	84.8

Table 1: Flow parameters for fixed laminar liquid injection ( $Re_l \simeq 1200$ ), varying the gas flow rate, in the vicinity of the transition in flapping orbit shapes. The gas Reynolds number is  $Re_g = 4Q_g/\sqrt{4\pi A_g}\nu_g$ , the gas-to-liquid dynamic pressure ratio is  $M = \rho_g U_g^2/\rho_l U_l^2$ , the liquid mass loading is  $m = \rho_l A_l U_l/\rho_g A_g U_g$  and the Weber number is based on the liquid diameter as  $We_{d_l} = \rho_g (U_g - U_l)^2 d_l/\sigma$ . The fluids are air and distilled water, at an ambient temperature of 25°C, with kinematic viscosities of  $\nu_g = 1.56 \cdot 10^{-5} \text{ m}^2 \text{ s}^{-1}$  and  $\nu_l = 8.96 \cdot 10^{-7} \text{ m}^2 \text{ s}^{-1}$ , densities  $\rho_g = 1.18 \text{ kg m}^{-3}$  and  $\rho_l = 996.9 \text{ kg m}^{-3}$ , surface tension  $\sigma = 72 \text{ mN m}^{-1}$ . For  $M = 5.3$ , 4 values of the swirl ratios are also considered:  $SR = 0$ , 0.25, 0.5 and 0.75.

are found roughly transverse to the gas flow. The bags are blown larger and larger until they break, producing very small droplets, while the rim yields larger drops. This atomization regime, a sub-regime of shear break-up, is referred to as bag break-up. For dynamic pressure ratio  $M \geq 5$  here, bag formation is also found on small-scale interfacial perturbations, that are initially observed to be roughly tangential to the liquid jet and are due to the Kelvin-Helmholtz instability. The perturbations are elongated and then stretched into bags along the liquid jets (in contrast to bags found towards the end portion of the liquid jet at lower values of  $M$  that are related to flapping).

## *2.2. Two-view high-speed imaging*

Similarly to the two-view approach of [19], two high-speed cameras are used to obtain back-lit imaging of the spray along two perpendicular projections. This is done by placing two bright sources of light behind the spray, each pointing toward a camera. The cameras are positioned in a horizontal plane and are orthogonal to each other (see Fig. 1b). Both cameras are synchronized and are triggered by the same input signal. A frame rate of 10 000  $Hz$  with duration of 1 s, an exposure time of 7  $\mu s$ , a resolution of 52  $\mu m$ /pixel, and a field of view of  $42 \times 34 \text{ mm}^2$  are used in the data collection. Both cameras capture orthogonal projections of the spray, leading to the ability to measure the 3D position of imaged objects, via a calibration step.

The imaging technique and image processing steps are identical to the ones described in [14]. Similarly, the liquid core length can be determined on each image as the longitudinal extent of the portion of the liquid jet that

is still attached to the nozzle. Each background-corrected image is nearly binary and assimilated to a phase indicator where black pixels correspond to liquid presence (and not mass). The liquid core corresponds then to the longest object which is still attached to the nozzle.

### 3. Skew normal distributions of the liquid core length

This section complements a previous contribution ([14]) to fully describe the statistics of the liquid core length of a laminar liquid jet surrounded by a turbulent gas jet, leading to atomization regimes from bag-break-up to fiber-type atomization. The probability density functions (PDF) of the liquid core were reported to deviate from Gaussian functions (positively skewed), but their shape were not parameterized. We introduce skew normal distributions, whose probability density functions can be expressed as follows:

$$PDF(x) = \frac{1}{\omega\sqrt{2\pi}} e^{-\frac{1}{2}\left(\frac{x-\xi}{\omega}\right)^2} \left[ 1 + \operatorname{erf} \left( \frac{\alpha(x-\xi)}{\sqrt{2}\omega} \right) \right] \quad (1)$$

where erf is the error function, and  $\xi$ ,  $\omega$ , and  $\alpha$  are 3 parameters respectively called location, scale, and shape parameter:

- Shape parameter,

$$\alpha = \left( \frac{2}{\pi} \left[ 1 + \left( \frac{4-\pi}{2\beta} \right)^{\frac{2}{3}} \right] - 1 \right)^{-\frac{1}{2}} \quad (2)$$

- Scale parameter,

$$\omega = \frac{\sigma}{\sqrt{1 - \frac{2\delta^2}{\pi}}} \quad (3)$$

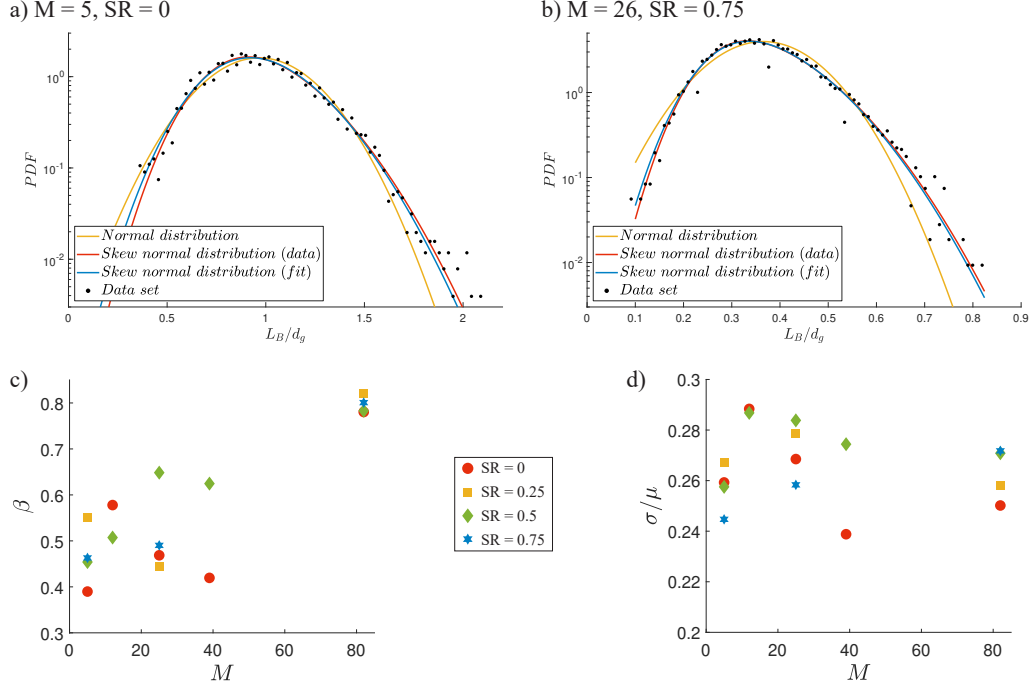


Figure 2: (color online) a-b) Comparison between normal and skew normal distributions (for the latter, both a fit and the parametric equation using moments calculated on the data are considered) of the liquid core length  $L_B$  for different values of  $M$  and  $SR$ . Evolution of the liquid core length skewness  $\beta$  (c) and ratio of standard deviation to mean  $\frac{\sigma}{\mu}$  (d) as a function of the gas-to-liquid dynamic pressure ratio  $M$ , for different swirl ratios  $SR$ .

- Location parameter,

$$\xi = \mu - \omega\delta\sqrt{\frac{2}{\pi}} \quad (4)$$

with  $\delta = \frac{\alpha}{\sqrt{1+\alpha^2}}$ . The parameters can be directly measured from the data using the first 3 standardized moments: mean  $\mu$ , standard deviation  $\sigma$  and skewness  $\beta$ .

Compared to normal distributions, the use of skew normal distributions results in significantly better modeling of the PDF of the liquid core length.

(see Fig. 2a). It provides a very good prediction of the liquid core behavior over the whole range of conditions studied. Moreover, the skew normal distribution derived from the mean, standard deviation, and skewness of the data set provides results very similar to those obtained by fitting a skew normal distribution on the PDF. The average relative error between the two is less than 4% over the entire data set studied, with 77% of the relative errors being less than 5% and the maximum error being 14%. This means studying the first 3 moments of the liquid core length data is enough to describe the entire statistics. Figure 2c) reports the skewness of the liquid core length, that was not reported previously. Note that a convergence study, taking 4 additional independent measurements, conducted on the condition  $M = 5$  (with and without swirl) lead to an estimation of the convergence error of about 10% on the skewness. It appears that, over the range  $5 < M < 80$  and irrespectively of the presence of swirl in the gas jet, no general trend is observed for the skewness. Higher values of the dynamic pressure  $M > 40$  seem to yield a skewness that is about 50% larger than lower values, indicating even higher probability to have larger lengths than smaller lengths with respect to the mean value. Note that over this whole range, the ratio of standard deviation to mean liquid core length is fairly constant with a value of approximately 25%, with no clear effect of the swirl ratio.

#### **4. Liquid distribution angle of the spray in the near field**

##### *4.1. Sliding average barycenters of the liquid phase*

The method proposed here is based on a simplification of the spray structure in the near-field, as only the movements of the bulk of the liquid are

studied and not the movements of individual features (e. g. ligament, drop). Therefore, the spray images are divided into 10 equal overlapping horizontal windows on which the barycenters of grey shades are calculated in order to determine the mean position of the liquid presence in each window (Fig. 3). As a shadowgraph only gives information about the presence or absence of liquid, and not about the quantity of liquid present, the barycenters are calculated by giving the same weight to all pixels are assigned to contain liquid (see [14]) instead of taking into account the grey intensity of each pixel. Moreover, an overlap between two consecutive windows of 33% is used to act as a sliding average over the variation of the barycenters' positions versus longitudinal distance  $x$ , while increasing the effective sampling resolution.

The position of the barycenter of each window is computed on each view (for any window at a downstream distance  $x$ , view 1 and 2 respectively yield  $y$  and  $z$ ) and is then used to obtain the 3D position of the liquid barycenters  $(x, y, z)$ , as described in Fig. 3a-c). This simplified three-dimensional representation of the spray is used to study the spatial and temporal evolution of the liquid jet flapping (including both its liquid core and some detached liquid inclusions without distinction).

Note that the liquid presence barycenter method with two-view back-lit imaging, while representing well the spatiotemporal dynamic of the bulk of the liquid phase in the near-field of a two-fluid coaxial atomizer, would not be adequate to describe the spray mid and far-field or phase objects of complex shape such as large deformed bubbles. In the former, the presence of small liquid droplets far from the centerline could for instance lead to overestimate weights in the barycenter computation compared to much larger drops close

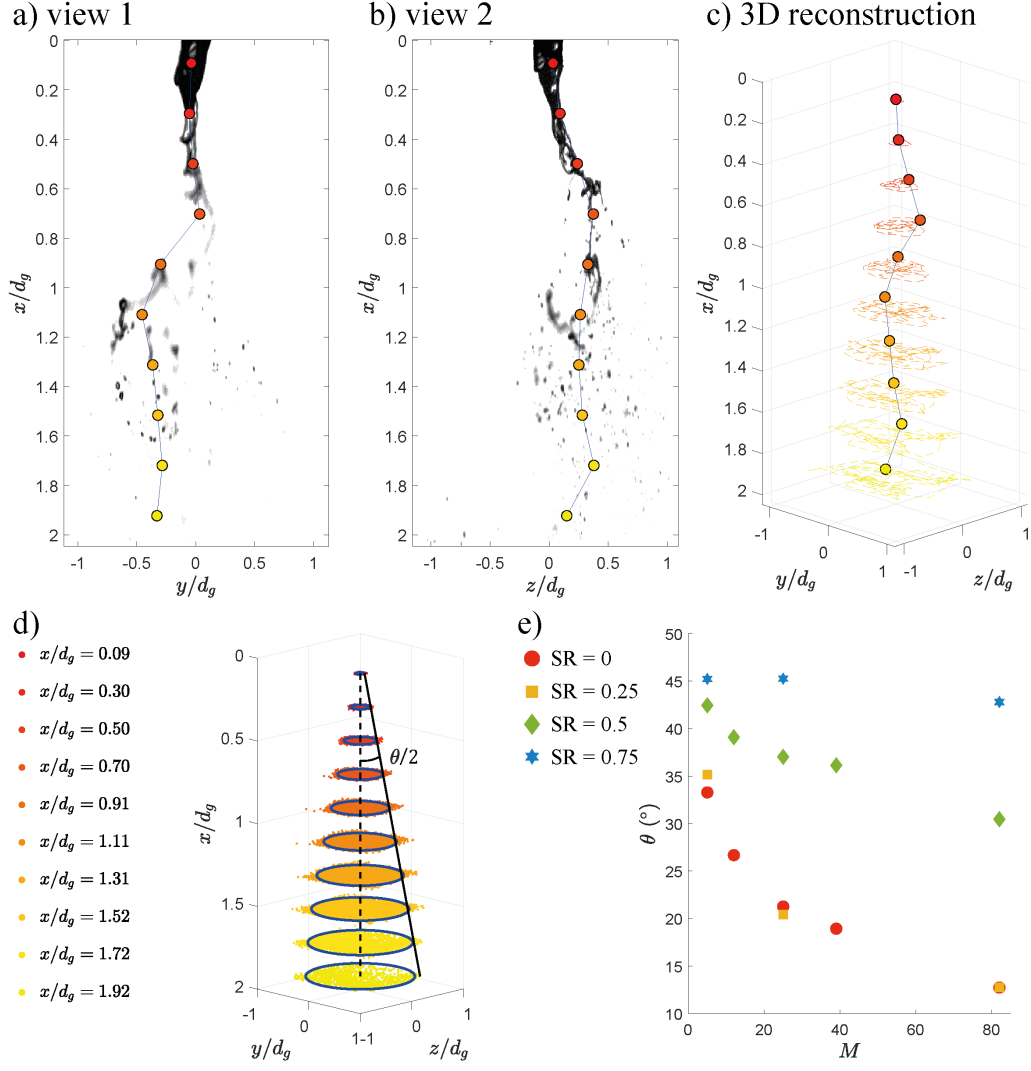


Figure 3: (color online) a-b) Typical synchronized snapshots from both views at  $M = 5$  and  $SR = 0.5$ , with associated detected liquid barycenters. c) 3D reconstruction of the barycenter overlayed over 200 subsequent detections (0.02 s, in dashed lines). d) Determination of the angle of the liquid distribution in the near-field of the spray based of the radii  $r_{95\%}$  (plotted in blue) that contain 95% of the barycenters in each transverse plane ( $SR = 0.5$  and  $M = 5$ ). The angle is then determined from the linear regression of  $r_{95\%}$  as a function of  $x/d_g$  (solid black line). e) Evolution of the liquid distribution angle  $\theta$  as a function of the gas-to-liquid dynamic pressure ratio  $M$ , for different swirl ratios  $SR$ .

to the center. In the latter, projected areas can be drastically overestimated, especially for non-convex shapes (see [20] for an in-depth discussion).

#### *4.2. Liquid distribution angle of the spray in the near field*

From the liquid barycenters method described above, a new metric is proposed to describe the spray expansion in the near field: the liquid distribution angle. By calculating the radii  $r_{95\%}$  that contain 95% of the barycenter positions at different downstream distance  $x$ , one can note a linear behavior. On this basis, the liquid distribution angle can then be defined from the linear regression of  $r_{95\%}$  as a function of  $x/d_g$  (see fig. 3d). Note that similar trends can be obtained by fitting the standard deviation of the barycenter positions  $\sigma_B$  as function of the downstream distance  $x/d_g$ . However, since the barycenter position distributions are not Gaussian, circles of radii  $2\sigma_B$  often cover areas that span more than all the barycenter positions (instead of 95.45% of the data set for a Gaussian).

Figure 3e shows the evolution of the liquid distribution angle with the gas-to-liquid dynamic pressure ratio  $M$  for different swirl ratios  $SR$ . For a constant dynamic pressure ratio  $M$ , one can observe that the liquid distribution angle increases with  $SR$ . Moreover, one can note that increasing the swirl ratio from 0 to 0.25 does not result in any significant changes in the liquid distribution angle, in qualitative agreement with previous work that shows the existence of a critical value for the swirl ratio above which swirl starts to affect the spray [11; 14]). On the other hand, for a constant swirl ratio  $SR$ , the liquid distribution angle decreases monotonically with  $M$ . This method complements the previous definition of initial spreading angle based on the liquid presence probability ([14]), with a weight put toward the lo-



cation of the bulk of the liquid (and less toward smaller liquid inclusions). Both methods yield trends that are qualitatively similar, and they both can be used to describe the rate at which the liquid redistributes spatially in the near-field of a coaxial atomizer, for comparisons between experiments and numerical simulations.

## 5. Transition in flapping orbit shapes

This section studies a sub-range of the operating parameters (see Table 1) where flapping can be identified without ambiguity. It uses the method introduced in Sec. 4 to obtain flapping orbits in 3D.

### 5.1. Definition of flapping orbits

The temporal and three-dimensional spatial evolution of the large-scale flapping instabilities occurring during the atomization is studied using the liquid barycenters method described above. In order to identify the flapping frequency, the power spectral densities (PSD) of the y-axis and z-axis position of each barycenter can be calculated from their time series obtained with this method (see Fig. 4a). Note that for high values of the dynamic pressure ratio (i. e. for high gas velocities here), flapping happens at high frequency [10]. Beyond  $M = 11$ , the peak in the PSD that corresponds to flapping is found in the high frequency range where a decaying power law is observed (see Fig. 4 beyond 300 Hz for instance), and a faithful determination of the dominant frequency becomes challenging. This was also the case for the determination of the shedding frequency based on the liquid core length time series in [14], where a typical timescale was retrieved using auto-correlation functions instead. Such determination would be easier using higher spatial

and temporal resolutions, which were not obtainable in the present work. In the following, the study hence focuses on the flapping morphology transition in the shear break-up regime of coaxial atomization for  $M \leq 11$ .

Once the main frequency  $f_0$  is determined as the PSD maximal peak, the 3D positions of all the barycenters (for each  $x$  position) are phase-averaged over many periods  $nT = n/f_0$  ( $n \geq 50$  and  $n \in \mathbf{N}$ ) and studied over an average complete flapping motion of duration  $T$  (Fig. 4b). This yields closed orbits, by definition, that correspond to the average motion of the liquid bulk along one flapping period  $T$ . As expected, the orbits extent increases with downstream distance as the flapping motion gains amplitude. The shape of the orbits does not appear however to change with downstream location, and is analyzed in Sec. 5.2. Note that orbits correspond here to the mean motion of the bulk of the liquid that is observed to happen at the flapping frequency. Instantaneous barycenter trajectories display high level of fluctuations, as can be observed in Fig. 3c (fluctuations of the barycenter positions are observed up to about  $0.75d_g$  from the centerline, while the mean flapping orbits only extent up to  $0.1d_g$ , Fig. 4b, in the example of  $M = 5$  and  $SR = 0.5$  at  $x = 1.5d_g$ ).

One can verify that the frequencies determined using the PSD indeed correspond to flapping motions by observing the motion of the liquid over a flapping period on both views (see Fig. 5 and the videos in Supplementary Materials in the case of  $M = 5$  and  $SR = 0.5$ ). This is checked for all conditions explored in this section, but at the lower range of dynamic pressure studied here, the flapping happens at low frequency (of the order of a few dozen to a few hundreds Hz), so the PSD always present a clear peak

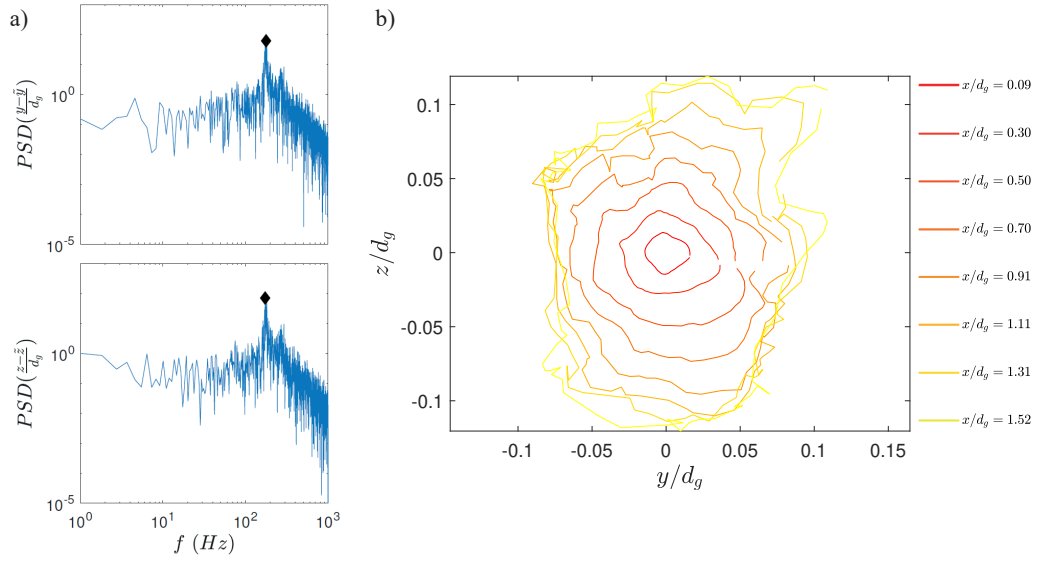


Figure 4: (color online) a) Power spectral densities (PSD) of the  $y$  and  $z$  positions (top and bottom) of the liquid barycenter for  $x/d_g = 0.5$ . The  $\blacklozenge$  symbols show the location of the maxima of the PSD, corresponding to the liquid jet flapping frequency. b) Flapping orbits obtained from the phase average at the measured flapping frequency of the liquid barycenters in each downstream plane. The condition displayed here is  $M = 5$  and  $SR = 0.5$ .

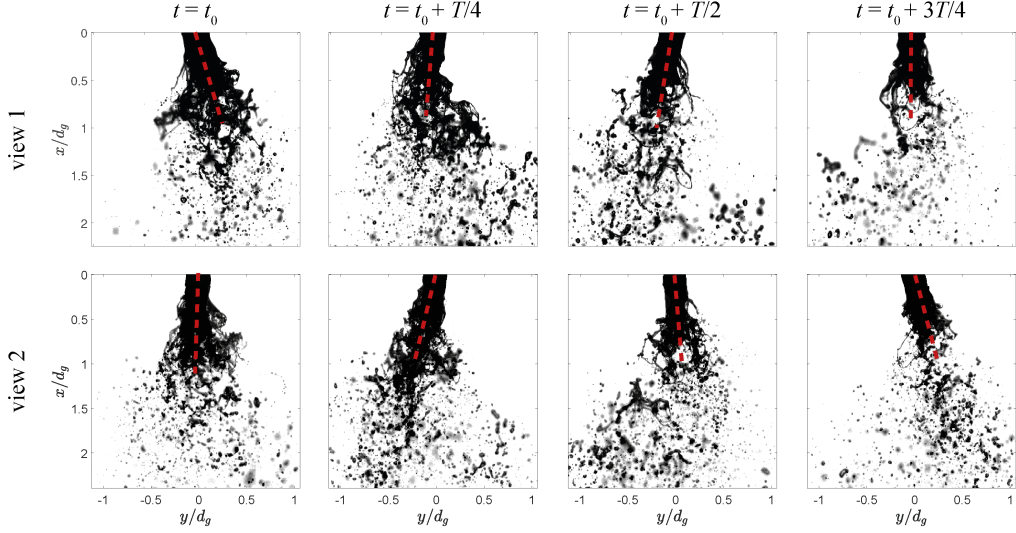


Figure 5: (color online) Instantaneous snapshots for both views spaced in time along a flapping period  $T$  determined from Fig. 4 ( $M = 5$ ,  $SR = 0.5$ ). The dashed lines' purpose is to guide the eyes through the flapping motion. The horizontal axes correspond to  $y$  for view 1 and  $z$  for view 2, normalized by  $d_g$ .

associated with flapping (unlike at high value of  $M$ , as discussed above).

Figure 4b) shows that, for a dynamic pressure ratio  $M = 5$  and a swirl ratio  $SR = 0.75$ , the phase-averaged barycenters have a quasi-circular motion around the axis of the atomizer, suggesting that the flapping motion also follows a circular pattern around the axis of the atomizer here. This is not the case for every sets of parameters studied, and especially at lower  $M$  and  $SR$  values. For instance, the case ( $M = 2$ ,  $SR = 0$ ) leads to a seemingly planar flapping, while the case ( $M = 5$ ,  $SR = 0$ ) results in a transitional state between planar and circular flapping, referred to as elliptical here (see Fig. 6). This transitional elliptical state is characterized by a circular motion of the barycenters close to the nozzle of the atomizer, which tends toward a

planar motion as they move away from it (or at least with a clear preferential direction, along  $z$  in this example). Note that for transitional orbits, there is a change in orbit shape as the downstream distance increases, as orbits close to the exit plane are found to be almost circular. Typical studies in the literature generally use only one camera. This work shows that this would lead to a biased measurements of the flapping amplitudes in cases where planar or transitional 2D-3D flapping is occurring. In the case of  $M = 5$  and  $SR = 0$ , the mean flapping amplitude along  $z$  can be estimated to be about 3 times larger than along  $y$  (which is here the largest error in flapping amplitude that could be made if a one-view measurement was performed along  $y$ , see Fig. 5b).

Videos in the Supplementary Materials are provided for the conditions shown in Fig. 6, depicting the positions along the orbits animated along a flapping period. The positions along the orbits present different angles in the  $(y, z)$  plane at a given time (i. e. with a phase difference between the orbits at different downstream positions  $x$  along the period). Beyond the transition, the flapping motion of the liquid jet is showed to be helical (and not circular), with and without swirl. Out-of-phase mean barycenter positions are also found the case for the planar flapping case, illustrating a meandering motion which oscillates in a plane (unlike a pendulum).

### 5.2. Quantifying orbit shapes

The shape of the flapping orbits are characterized quantitatively by using a shape factor defined using the orbit perimeter  $P$  and area  $A$  as  $P/2\sqrt{\pi A}$ , which equals to 1 for a circle. The shape factor for the planar, ellipsoidal and circular orbits from Fig. 6a, b and c) are approximately 5.36, 1.41 and

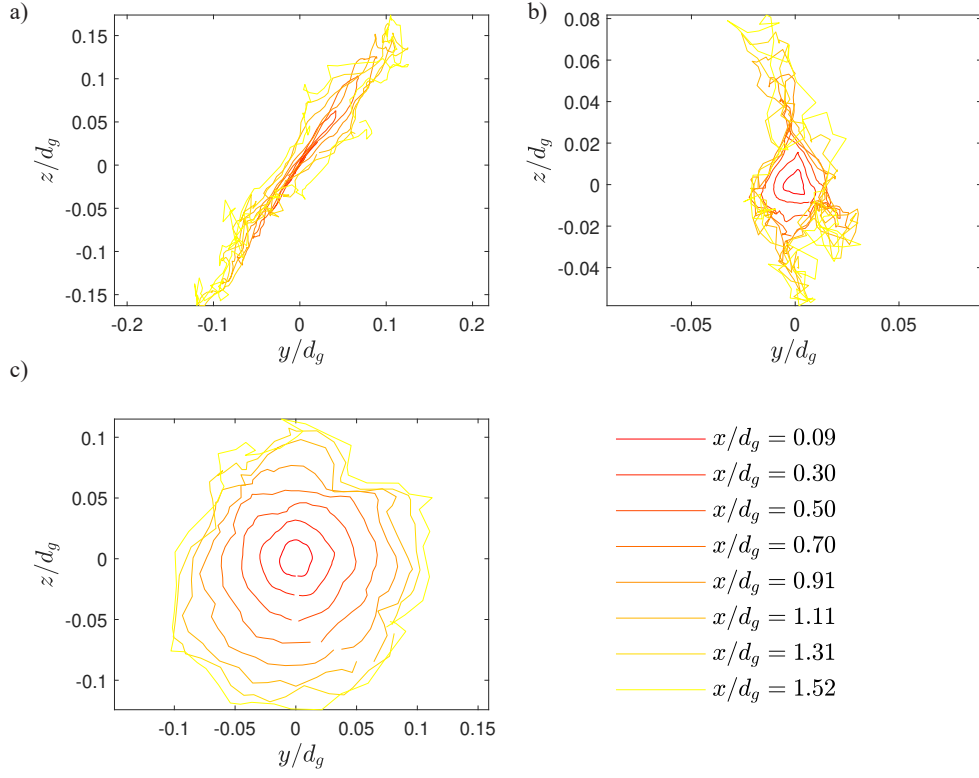


Figure 6: (color online) Flapping orbits displaying different shapes obtained for  $M = 2$  (a, planar),  $M = 5$  (b, ellipsoidal) without swirl, and for  $M = 5$  and  $SR = 0.75$  (c, circular).

1.02. The shape factor values are obtained by averaging the shape factor for the 3 orbits sampled at  $x/d_g = 0.09, 0.3$  and  $0.5$  to increase accuracy, with a standard deviation corresponding to the convergence error on the three measurements. Only the first 3 sampled downstream locations are used here, as the orbit shapes become noisier at larger values of  $x$  (which leads to overestimation of the perimeter values), especially at higher values of  $M$  and  $SR$ , where the liquid core length shortens and the barycenter would only represent detached liquid inclusions. Figure 7a-b) shows the shape factor evolution along  $M$  ( $SR = 0$ ) and along  $SR$  ( $M = 5$ ) respectively. Without swirl, increases of dynamic pressure ratio rapidly lead to transition from planar to ellipsoidal orbits and atomization in the bag break-up regime always displays ellipsoidal orbits here (while low  $M$  regimes just beyond the bag-less shear break-up regime are planar). However, at these intermediate dynamic pressure ratio values, no circular orbit is observed without swirl addition ( $P/2\sqrt{\pi A} = 1.13$  for  $M = 11$  and  $SR = 0$ ). When swirl is added beyond the critical swirl ratio (so for  $SR \geq 0.5$  here), the orbits are immediately quasi-circular, with a shape factor close to one.

Alternatively, similar conclusions can be reached by simply measuring the maximal extend of the orbits  $r_{max}$  (Fig. 7c-d). Normalizing  $r_{max}$  by the longitudinal distance  $x$  is enough to collapse the plots from the 3 sampled locations, in agreement with the linear spreading of the liquid observed in Fig. 3d). The orbit maximal radius also serves as a proxy for the flapping amplitude, only measured along its preferential direction for planar and ellipsoidal flapping modes (i. e. corresponding to the maximal and not azimuthally averaged flapping amplitude). It shows that larger values of the

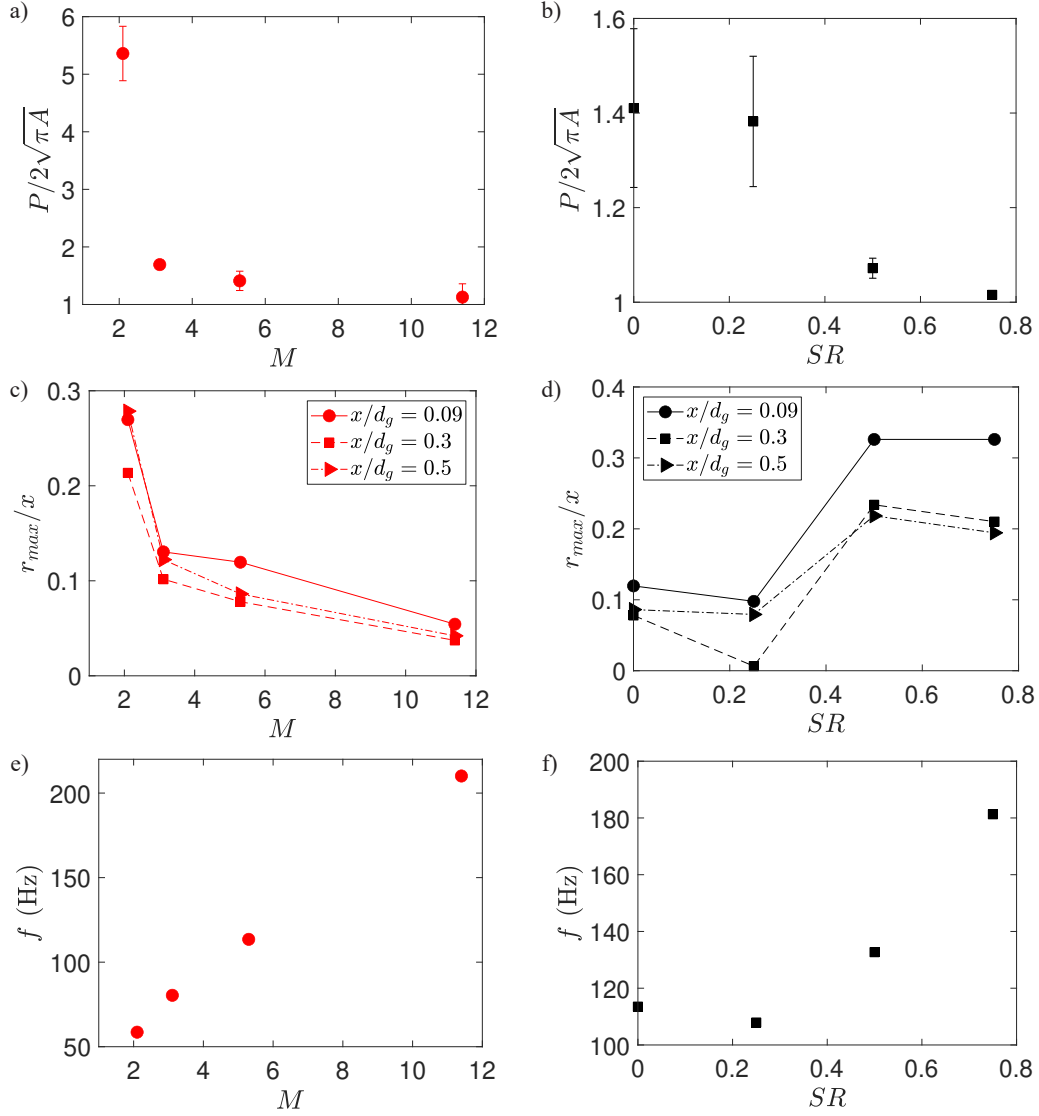


Figure 7: (color online) Shape factor obtained from the orbit measured perimeters  $P$  and area  $A$  without swirl as a function of  $M$  (a), and for  $M = 5$  as a function of  $SR$ . The shape factor is averaged over three downstream locations  $x/d_g = 0.09, 0.3$  and  $0.5$ , and the errorbars correspond to the convergence error. Similarly, c-d) and e-f) display the flapping amplitude measured through the orbit maximal radii  $r_{max}$  (at three downstream distances) and the flapping frequencies  $f$ .



gas-to-liquid dynamic pressure ratio yield smaller amplitudes, in agreement with the shorter liquid core lengths, and that the presence of swirl increases the flapping amplitude. For the latter, a factor of about 2 is measured, placing the amplitude at  $M = 5$  and  $SR = 0.75$  almost at the level of the large-amplitude planar flapping motion observed at  $M = 2$  without swirl.

As already demonstrated in the literature (see [10]), the flapping frequency increases when the dynamic pressure ratio  $M$  increases. This work shows that it also increases with the swirl ratio. Once again, one can note that there are no significant changes between  $SR = 0$  and  $SR = 0.25$ , for a constant  $M$ . The increased flapping frequency in the presence of swirl beyond a critical swirl ratio is compatible with previous findings concerning faster timescales of the interfacial instability dynamics [21]. Higher flapping frequencies in the presence of swirl were also reported recently in a wider range of dynamic pressure ratios and several liquid Reynolds numbers [17].

## 6. Discussion

A first glance at the spray in the near-field, even when using two perpendicular transverse views, leads to an axisymmetric statistical description of the spray. The angle defined using the liquid barycenters indeed smooth out the potential existence of a preferential direction, and similar results would be obtained if only the moments of the barycenters were used. While this still gives a relevant representation on how the liquid is redistributed by the gas jet in the near-field, allowing for a good comparison between different operating conditions, it lacks the accuracy that is necessary to precisely quantify the liquid distribution and to build models and predictions. While other

methods could be used, such as geometric fits of the 2D transverse scatter plots or of 2D transverse probability density functions of the barycenter, the use of phase averaging to determine flapping orbits prove itself to be a simple way to yield a quantitative picture of the liquid mean motion over a flapping period. This representation focuses on the location of the bulk of the liquid in space and time. The phase-averaged closed orbits directly evidence that flapping can have a strong preferential direction, with shape factors larger than 5 (i. e. motions along the preferential direction of about 50 times larger than motions along the direction perpendicular to the preferential direction), with strongly anisotropic liquid flux distributions in the far-field. These observations result from an experimental realization per condition, representing measurements over many flapping periods (50 to 200).

Note that the transition in flapping orbit shape does not seem to affect the scaling law of the flapping frequency. The growth of the frequency with dynamic pressure ratio is indeed monotonous and in good agreement with previously reported data (e. g. [10]). This indicates that the mechanism governing the flapping characteristic timescale, and the one determining flapping orbits shape are independent from each other. Furthermore, while the shape of the flapping orbit changes drastically, becoming quasi-circular as soon as swirl is added beyond the critical value at which swirl actually affects the spray,  $SR \geq 0.5$ , the flapping frequency gradually increases with swirl addition. Further study on the effect of the swirl ratio and on a larger range of dynamic pressure ratios would be interesting to determine the scaling law as a functions of both  $M$  and  $SR$ . On the other hand, the transition in flapping shape has an effect on the flapping amplitude, measured here as the point of

the orbit found furthest from the spray axis along an average flapping trajectory. As flapping goes from a planar to a transitional quasi-circular shape when  $M$  increases, the flapping amplitudes gradually decreases, by a factor of about 3 when  $M$  goes from 2 to 11. However, swirl addition, that leads to quasi-circular orbits also increases the flapping amplitude. The increase, similarly to the change of shape factor, is seen abruptly for  $SR \geq 0.5$  in opposition to the gradual increase in flapping frequency. This means that the flapping amplitude for both  $SR = 0.5$  and  $0.75$  is roughly the same, approximately 2 to 3 times the one observed without swirl. Lesser amplitude at high dynamic pressure values are compatible with shorter liquid core lengths compared to lower  $M$ , which could lead to large-scale interactions with the gas jet. When swirl is added, the liquid core length is further reduced at a given  $M$  [14], but the azimuthal component of the gas jet creates an additional radially outward pressure term that could lead to larger flapping amplitudes. This is compatible with the wicking dynamic of the liquid jet, which can be observed to wet the outer wall of the liquid nozzle (up to about 0.4 mm upstream of the exit plane, i. e. approximately  $d_l/5$  or  $(D_l - d_l)/2$ ) using X-ray radiography [16]. Note that wicking may play a role in the transition in flapping orbit shape as it drastically modifies the initial condition of the gas-liquid interface. In conclusion, swirl addition leads to flapping motions at both higher amplitudes and frequencies compared to non-swirled gas jet. At moderate dynamic pressure ratio, where primary break-up events can result from both interfacial instabilities and the large-scale flapping instability, such increased flapping energy could indicate a greater role of flapping in the spray formation mechanisms for these operating conditions.

The transition in flapping shape is reached for  $M = 5$  here, with the shape parameter falling below 1.5. This operating condition corresponds to a Weber number, based on the inlet velocity differences between each phase  $U_g - U_l$  and on the liquid inner diameter  $d_l$ , of  $We_{d_l} = 39.1$ . This value is very close to the one reported for transition between shear break-up and bag-break-up: the phase diagram of qualitative atomization regimes from [1] points toward a transition around  $We_{d_l} = 40$  for the laminar liquid Reynolds number  $Re_l = 1200$ . However, in the current range of operating conditions for this atomizer, bags are observed even at the lower Weber number value explored of  $We_{d_l} = 15.4$  (see Fig. 8a-b, corresponding alternatively to  $M = 2$ ). In this case, as the liquid core meanders due to the flapping instability, bags are blown in the last portion of the jet, where the liquid resembles a hook shape. The bottom of this hook presents a region that is transverse to the gas jet which stretches it into a thin membrane that is referred to as a bag. On the other hand, for  $We_{d_l} \geq 39.1$ , another mechanism leads to the formation of bags. Small-scale interfacial instabilities, namely shear-driven Kelvin-Helmholtz, produce interfacial perturbations that once elongated by the gas stresses, can be blown into bags that are attached to the side of the liquid core (see Fig. 8c-d). These bags coexist with the ones originating from the large-scale flapping instability (Fig. 8c-d is for instance taken right after the rupture of such a bag, and the larger drops resulting from the rim are visible on the snapshots. Movies in Supplementary Materials illustrate the difference in bag formation and liquid core morphologies for both of these conditions ( $M = 2$  and  $M = 5$ ). It appears that the described transition between (bag-less) shear break-up and (shear) bag break-up described in [1]

onsets earlier here, and that the prescribed transition around  $We_{d_l} = 40$  is more closely related to the relative role between large-scale and small-scale instabilities becoming more or less comparable in bag formation. The difference in the transition value of  $We_{d_l}$  between the present work and the proposed transition in [1] could be due to subtle dependencies in the atomizer geometry. In particular, while the inlet liquid diameter  $d_l$  is expressed linearly in  $We_{d_l}$ , the ability of the gas to stretch the elongated liquid jet could depend non-linearly on this quantity. This hypothesis would however need to be further investigated in a liquid Reynolds number - gas Weber number parameter space that also includes variable atomizer geometry.

For both low and intermediate values of dynamic pressure ratio, the flapping orbits shape is either planar or elliptical, displaying a strong preferential direction. This is a strong deviation from the axisymmetric inlet conditions related to the coaxial two-fluid atomizer, and the shape is only found to be invariant through rotation of  $\pi$  around the atomizer axis. At higher momentum ratios, or in the presence of swirl, axisymmetry is regained. The profile shape and flapping direction can roughly be described as belonging to the symmetry group  $SO(2)$ . Note that for  $M = 11$ , the shape factor is equal to 1.13, corresponding to a ratio of the major to minor axes of 1.2, while the smallest shape factor found is at  $M = 5$  and  $SR = 0.75$  with a value of 1.02 (ratio of the major to minor axes of 1.08). These slight deviations from axisymmetry, probably close to the uncertainty of the shape factor of a finite-sample orbit, can be considered negligible, even when compared to the shape factor value of 1.4 for  $M = 5$  without swirl. For  $M \leq 5$ , the strong departure from axisymmetry is expected to have consequences on the liquid-

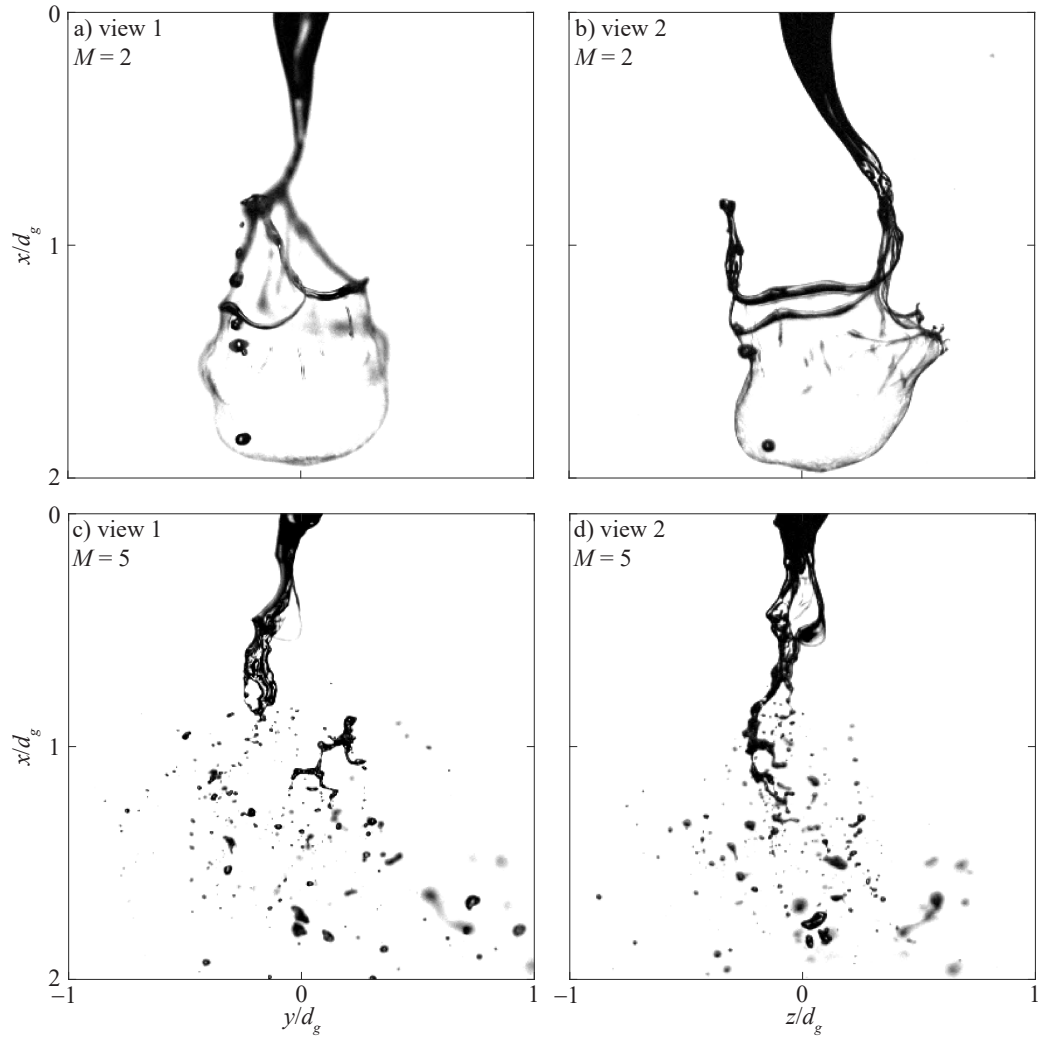


Figure 8: Snapshot displaying bag formation originating from the large-scale flapping instability at  $M = 2$  (a-b) and from a small-scale interfacial instability at  $M = 5$  (c-d).

gas interactions and primary break-up in the near-field, as well as transport and secondary break-up further downstream. This needs to be accounted for when taking measurements in the far-field or establishing predictions of spray characteristics, and also possibly in modeling approaches (e. g. spatio-temporal linear stability analysis).

The transitional elliptical shape (Fig. 6b) indicates a strong preferential direction, here along  $z$ , with deviations along  $y$  only when the liquid bulk is located closer to the centerline (at small radial distances). In the absence of bag formation along the liquid jet (i. e. bags only originating from flapping and located approximately in the last third of the liquid core), at  $M = 2$ , the liquid bulk flaps back and forth in a plane. The liquid core mostly corresponds to a twisted liquid column which experiences regular fragmentation associated with bag break-up. The rupture at the most stretched portion of the bag propagates up to the rim and break the liquid jet tip altogether. In contrast, at  $M = 5$ , bag formation can also originate from small-scale interfacial instabilities, and partial break-up of the liquid jet happens before the end of the liquid jet. While a bag is inflated, despite representing a very small portion of the liquid mass as the membrane is very thin, it offers a large increase in the aerodynamic drag experienced by the liquid jet (acting like a spoiler). The formation of bags from small-scale interfacial instabilities tend to be associated with a liquid core and detached liquid bulk mostly aligned with the centerline. On the other hand, the bags happening at the extrema of the flapping period are associated with twisted liquid jets, that remain thin up to their tip where the bag is formed. The presence of bags close to the nozzle (at a few liquid diameters), offers a thick liquid column that is sus-

pected to yield additional drag, which could oppose large-amplitude flapping in a preferential direction. It is likely that the emergence of this added drag around  $M = 5$  is what leads to the transition in flapping dynamics. This phenomenon results in the region of  $r < 0.02d_g$  in Fig. 6b) which bounds all of the flapping orbits at the downstream distances sampled. At low dynamic pressure ratio (planar flapping) or with swirl (circular flapping), such region does not exist as the liquid core’s main direction strongly deviates from the centerline.

## 7. Conclusions

Using high-speed two-view back-lit imaging, the spatio-temporal evolution of the spray in the near-field of a two-fluid coaxial atomizer with tunable gas swirl has been characterized.

First, a parametric description of the liquid core length probability density functions has been introduced. It consists in a skew normal distribution, whose 3 parameters are directly computed from the mean, standard deviation and skewness of the liquid core length time series. This parametrization has been shown to represent the data very well over a wide range of gas-to-liquid dynamic pressure and gas swirl ratios ( $5 < M < 80$  and  $0 < SR < 0.75$ ). The skewness and ratio of standard deviation to mean liquid core length were also reported for completeness, showing a not insignificant degree of spread but no clear trends with these parameters.

Second, a method was introduced to measure the 3D barycenter time series of the bulk of the liquid. This yielded a simple and robust definition of the liquid distribution angle of the spray in the near-field, which as ex-



pected decreases with gas-to-liquid dynamic pressure ratio  $M$  and increases with swirl ratio  $SR$ , beyond a critical value in agreement with the literature. The method, which does not require any significant image processing, gives access to the transverse motions of the liquid and hence to flapping frequency measurements. Phase-averaging of the liquid motion along the measured flapping periods led to the determination of mean flapping orbits along various transverse planes at growing downstream distance. The shapes of the orbits were found to be invariant with distance (except for transition orbit shapes), but showed changes throughout the parameter space: planar motions were exhibited at low dynamic pressure ratio, while quasi-circular motions were found for either higher ratios and/or in the presence of swirl. This was quantified using a shape factor, defined from the orbits perimeter and area. The flapping amplitudes, measured along the flapping preferred direction when it existed, follow a similar trend than the flapping shape with  $M$ , but the opposite trend with  $SR$ . This means that at high  $M$  values, the flapping amplitude is lower than at low values, but it increases when swirl is added ( $SR \geq 0.5$ ). The flapping frequency did not seem to be dependent on the flapping shape, increasing with dynamic pressure ratio, but was found to also increase in the presence of swirl.

The transitions in flapping orbit shapes seems to be related to the occurrence of bag formation along the liquid jet, on interfacial perturbations that originates from small-scale interfacial instabilities. In the absence of bags along the liquid jet, it seems that any deviation from the centerline from the liquid jet (probably triggered by a large-scale gas fluctuation) is countered by an opposing aerodynamic force as the liquid enters the high-speed gas.

The liquid jet may then experience back-and forth motions in a plane whose orientation may originate from a given initial perturbation, as the liquid jet does not present any significant interfacial perturbation at low dynamic pressure ratio. Further investigations, at higher temporal and spatial resolution, for larger gas-to-liquid dynamic pressure ratios, should be conducted to determine what is the evolution of the flapping shape from bag break-up to fiber-type atomization, and how swirl affects the flapping instability at high  $M$ . Measurements of the droplet population in the far-field throughout the cross-section of the spray should be considered to assess the spatial heterogeneities in the presence of non-axisymmetric flapping. An additional open-question is the origin and potential reproducibility of the preferential flapping direction. Note that the exhibited preferential direction is observed to be different at different operating conditions (see Fig. 6). Besides consequences on the far-field spray statistics, this could be important to evaluate real-time spray features, such as is done when implementing atomization feedback control [22; 23].

## 8. Acknowledgements

This work was sponsored by the Office of Naval Research (ONR) as part of the Multidisciplinary University Research Initiatives (MURI) Program, under grant number N00014-16-1-2617. The views and conclusions contained herein are those of the authors only and should not be interpreted as representing those of ONR, the U.S. Navy or the U.S. Government.

## References

- [1] J. C. Lasheras, E. Hopfinger, Liquid jet instability and atomization in a coaxial gas stream, *Annual review of fluid mechanics* 32 (1) (2000) 275–308.
- [2] C. Dumouchel, On the experimental investigation on primary atomization of liquid streams, *Experiments in fluids* 45 (3) (2008) 371–422.
- [3] P. Marmottant, E. Villermaux, On spray formation, *Journal of fluid mechanics* 498 (2004) 73–111.
- [4] H. Eroglu, N. Chigier, Z. Farago, Coaxial atomizer liquid intact lengths, *Physics of Fluids A: Fluid Dynamics* 3 (2) (1991) 303–308.
- [5] M. P. Juniper, S. M. Candel, The stability of ducted compound flows and consequences for the geometry of coaxial injectors, *Journal of Fluid Mechanics* 482 (2003) 257–269.
- [6] C. M. Varga, J. C. Lasheras, E. J. Hopfinger, Initial breakup of a small-diameter liquid jet by a high-speed gas stream, *Journal of Fluid Mechanics* 497 (2003) 405–434.
- [7] W. Mayer, R. Branam, Atomization characteristics on the surface of a round liquid jet, *Experiments in fluids* 36 (4) (2004) 528–539.
- [8] B. Leroux, O. Delabroy, F. Lacas, Experimental study of coaxial atomizers scaling. part i: dense core zone, *Atomization and Sprays* 17 (5) (2007).

- [9] G. Charalampous, Y. Hardalupas, A. Taylor, Structure of the continuous liquid jet core during coaxial air-blast atomisation, *International Journal of Spray and Combustion Dynamics* 1 (4) (2009) 389–415.
- [10] A. Delon, A. Cartellier, J.-P. Matas, Flapping instability of a liquid jet, *Physical Review Fluids* 3 (4) (2018) 043901.
- [11] E. Hopfinger, J. Lasheras, Explosive breakup of a liquid jet by a swirling coaxial gas jet, *Physics of Fluids* 8 (7) (1996) 1696–1698.
- [12] V. McDonell, M. Adachi, G. Samuelsen, Structure of reacting and non-reacting swirling air-assisted sprays, *Combustion science and technology* 82 (1-6) (1992) 225–248.
- [13] Y. Hardalupas, J. Whitelaw, Coaxial airblast atomizers with swirling air stream, *Recent advances in spray combustion: Spray combustion measurements and model simulation*. 2 (1996) 201–232.
- [14] N. Machicoane, G. Ricard, R. Osuna-Orozco, P. D. Huck, A. Aliseda, Influence of steady and oscillating swirl on the near-field spray characteristics in a two-fluid coaxial atomizer, *International Journal of Multiphase Flow* 129 (2020) 103318. doi:10.1016/j.ijmultiphaseflow.2020.103318.
- [15] P. Billant, J.-M. Chomaz, P. Huerre, Experimental study of vortex breakdown in swirling jets, *Journal of Fluid Mechanics* 376 (1998) 183–219.
- [16] N. Machicoane, J. K. Bothell, D. Li, T. B. Morgan, T. J. Heindel, A. L. Kastengren, A. Aliseda, Synchrotron radiography charac-

- terization of the liquid core dynamics in a canonical two-fluid coaxial atomizer, *International Journal of Multiphase Flow* 115 (2019) 1–8. doi:10.1016/j.ijmultiphaseflow.2019.03.006.
- [17] A. Kumar, S. Sahu, Large scale instabilities in coaxial air-water jets with annular air swirl, *Physics of Fluids* 31 (12) (2019) 124103.
  - [18] N. Machicoane, A. Aliseda, Experimental characterization of a canonical coaxial gas-liquid atomizer, *Institute for Liquid Atomization and Spray Systems. ILASS 2017, 29th Annual Conference on Liquid Atomization and Spray Systems*, Atlanta, GA, USA, May 15-18 (2018).
  - [19] J.-P. Matas, A. Cartellier, Flapping instability of a liquid jet, *Comptes Rendus Mécanique* 341 (1-2) (2013) 35–43.
  - [20] A. U. M. Masuk, A. Salibindla, R. Ni, A robust virtual-camera 3d shape reconstruction of deforming bubbles/droplets with additional physical constraints, *International Journal of Multiphase Flow* 120 (2019) 103088.
  - [21] G. Ricard, N. Machicoane, R. Osuna-Orozco, P. D. Huck, A. Aliseda, Role of convective acceleration in the interfacial instability of liquid-gas coaxial jets, *Physical Review Fluids* 6 (8) (2021) 084302. doi:10.1103/PhysRevFluids.6.084302.
  - [22] R. Osuna-Orozco, N. Machicoane, P. D. Huck, A. Aliseda, Feedback control of coaxial atomization based on the spray liquid distribution, *Atomization and Sprays* 29 (6) (2019) 545–551. doi:10.1615/AtomizSpr.2019031766.

- [23] R. Osuna-Orozco, N. Machicoane, P. D. Huck, A. Aliseda, Feedback control of the spray liquid distribution of electrostatically assisted coaxial atomization, *Atomization and Sprays* 30 (1) (2020) 1–9. doi: 10.1615/AtomizSpr.2020033430.